

Sublayers Editing of Covalent MAX Phase for Nanolaminated Early Transition Metal Compounds

Ziqian Li ^{1,2}, Ke Chen ^{1,3*}, Xudong Wang ^{1,2}, Kan Luo ¹, Lei Lei ^{1,3}, Mian Li ^{1,3}, Kun Liang ^{1,3}, Degao Wang ^{1,3}, Shiyu Du ¹, Zhifang Chai ^{1,3}, Qing Huang ^{1,3*}

¹ Zhejiang Key Laboratory of Data-Driven High-Safety Energy Materials and Applications, Ningbo Key Laboratory of Special Energy Materials and Chemistry, Ningbo Institute of Materials Technology and Engineering, Chinese Academy of Sciences, Ningbo 315201, China.

² University of Chinese Academy of Sciences, Beijing 100049, China.

³ Qianwan Institute of CNiTECH, Ningbo 315336, China.

*Correspondence to:

Prof. Ke Chen, E-mail: chenke@nimte.ac.cn

Prof. Qing Huang, E-mail: huangqing@nimte.ac.cn

Abstract: Two-dimensional transition metal carbides and nitrides (MXenes) have gained popularity in fields such as energy storage, catalysis, and electromagnetic interference due to their diverse elemental compositions and variable surface terminations (T). Generally, the synthesis of MXene materials involves etching the weak M-A metallic bonds in the ternary layered transition metal carbides and nitrides (MAX phase) using HF acid or Lewis acid molten salts, while the strong M-X covalent bonds preserve the two-dimensional framework structure of MXenes. On the other hand, the MAX phase material family also includes a significant class of members where the A site is occupied by non-metal main group elements (such as sulfur and phosphorus), in which both M-A and M-X are covalent bond-type sublayers. The aforementioned etching methods cannot be used to synthesize MXene materials from these parent phases. In this work, we discovered that the covalent bond-type M-A and M-X

sublayers exhibit different reactivity with some inorganic materials in a high-temperature molten state. By utilizing this difference in reactivity, we can structurally modify these covalent sublayers, allowing for the substitution of elements at the X site (from B to Se, S, P, C) and converting non-metal A site atoms in non-*van der Waals* (non-*vdW*) MAX phases into surface atoms in *vdW* layered materials. This results in a family of early transition metal Xide chalcogenides (TMXCs) that exhibit lattice characteristics of both MXenes and transition metal chalcogenides. Using electron-donor chemical scissors, these TMXC layered materials can be further exfoliated into monolayer nanosheets. The atomic configurations of each atom in these monolayer TMXCs are the same as those of conventional MXenes, but the oxidation states of the M-site atoms can be regulated by both X-site atoms and intercalated cations. This has significant implications for applications in electrochemical energy storage and surface catalysis.

The MAX phases, with the chemical formula $M_{n+1}AX_n$, represent a large class of non-van der Waals layered ternary materials. In these compounds, M stands for an early transition metal, A is a main group or subgroup element, and X comprises carbon, nitrogen, and/or boron. The value of n is typically 1 or 2. From the perspective of layered crystal structure and chemical bonding, MAX phases can be viewed as alternating stacks of M-X and M-A sublayers along the c-axis. In the M-X sublayer, strong covalent bonds form between transition metals and nonmetal elements, while the M-A sublayer features weak metallic bonds between transition metals and main group elements such as Al and Si. By exploiting the different chemical reactivities of the two sublayers, selective chemical etching can be conducted. For example, metal A atoms in the M-A sublayer will easily lose electrons and be preferentially etched away in a proton-containing solution or Lewis acid molten salts, while the chemically-inert covalent M-X sublayer keep intact and preserve its two-dimensional structure. This selective sublayer etching process results in the creation of diverse two-dimensional *vdW* early transition metal carbides and nitrides (MXenes).

In MAX phases, not only do the [M-X] sublayers consist of covalent $[M_6X]$ octahedron, but the p orbitals of A-site chalcogens can also exhibit strong coupling with the d orbitals of M-site elements due to the high electronegativity of chalcogens, as observed in bonds such as Ti-S, Zr-S, Zr-Se, Hf-S, Hf-Se, and Hf-Te within the phases Ti_2SC , Zr_2SC , Hf_2SC , Nb_2SC , Zr_2SB , Hf_2SB , Nb_2SB , Zr_2SeC , Hf_2SeC , Zr_2SeB , Hf_2SeB , and Hf_2TeB ¹⁸⁻²². The disparity between M-A bonds and M-X bonds is significantly smaller than that typically found in MAX phases, which contain both metallic and covalent bonds. Consequently, LAMS is ineffective against stripping such stable covalent bonds. In this work, the reactive difference between covalent [M-A] sublayers and covalent [M-X] sublayers is exploited and recognized. A covalent

chemical scissor is introduced to selectively edit the covalent [M-B] sublayers within boride MAX phases. The customized X elements of MAX phases are orderly substituted from B, Se, S, P, to C. The resulting transition metal Xide-chalcogenides (TMXC) with unconventional X elements, derived from the covalent-sublayer edited MAX phase precursors, facilitate the discovery of a series of nanolaminated early transition metal compounds, thereby significantly broadening the spectrum of available 2D materials.

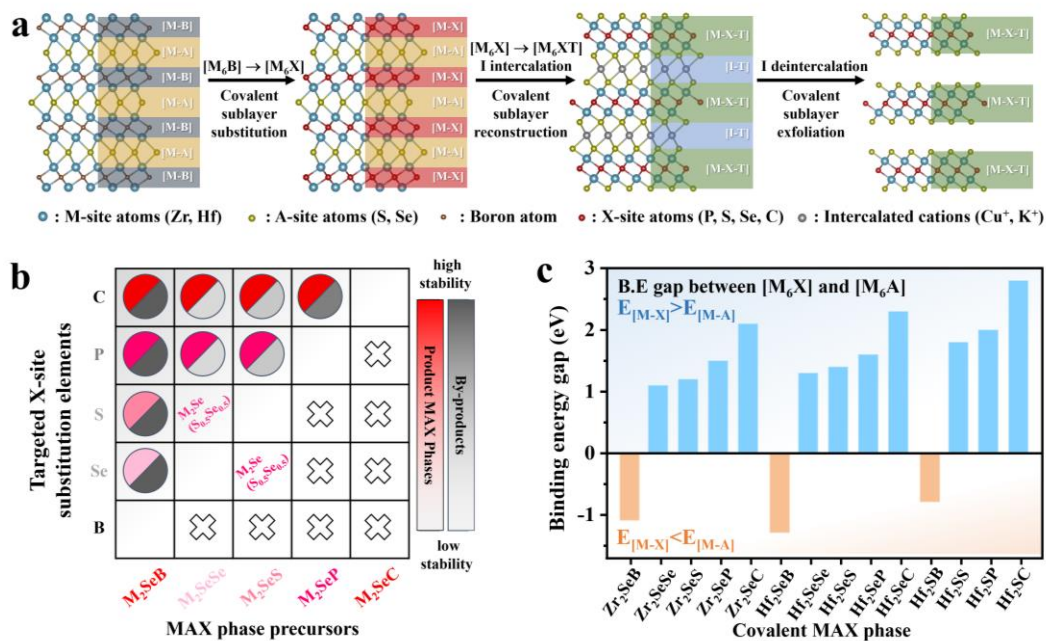


Fig. 1. Structural editing policy of covalent MAX phases and *i*-TMXC. **(a)** Schematic representation of the transformation from the covalent boride MAX phases to 2D TMXC nanosheets. **(b)** An illustration depicting the concept of substitution in covalent [M-X] sublayers within MAX phases. **(c)** The variations in the binding state of the M element within $[M_6X]$ and $[M_6A]$ configurations of the covalent MAX phase, as analyzed through XPS, whose X site represents B, Se, S, P, and C.

Fig. 1 shows the topochemical transformation from the covalent boride MAX phases to TMXC nanosheets with three sequential reaction steps: (i) the substitution of boron in the [M-B] sublayers of boride MAX phases with non-metallic atoms, facilitated by covalent chemical scissors, which reduces the Gibbs free energy due to the formation of more stable M-X covalent bonds within the MAX phases and/or the

generation of ultra-stable byproducts; (ii) the intercalation of cations into the MAX phases precursor, resulting in the reconstruction of covalent [M-X-T] sublayers in the ion intercalated TMXC (*i*-TMXC); (iii) the exfoliation of the covalent [M-X-T] sublayers within *i*-TMXC through electron injection using metallic chemical scissors in an alkali molten salt environment, and the further delamination of the accordion-like alkali metal intercalated TMXC through the progressive oxidation of protons and sonication, ultimately yielding 2D TMXCs (*d*-TMXC).

The stability of transition metal compounds, which is predominantly influenced by the characteristics of chemical bonding, elucidates the transformation among boride MAX phases, selenide MAX phases, sulfide MAX phases, phosphide MAX phases, and carbide MAX phases (Fig. 1b and S1). It is noteworthy that unconventional elements such as Se, S, and P have been incorporated into the X site of MAX phases, alongside the more prevalent C and B. Furthermore, the differing valence states of metallic elements when interacting with non-metallic elements in the [M-X] and [M-A] sublayers can be leveraged to facilitate the intercalation of cations into covalent MAX phase, thus resulting in the reconstruction of the [M-X-T] sublayers (Fig. 1c). Additionally, dual anionic early transition metal compounds have been intercalated with Cu, Li, Na, and K atoms. Detailed experimental data and findings that substantiate these phases are presented in Tables S1-S4.

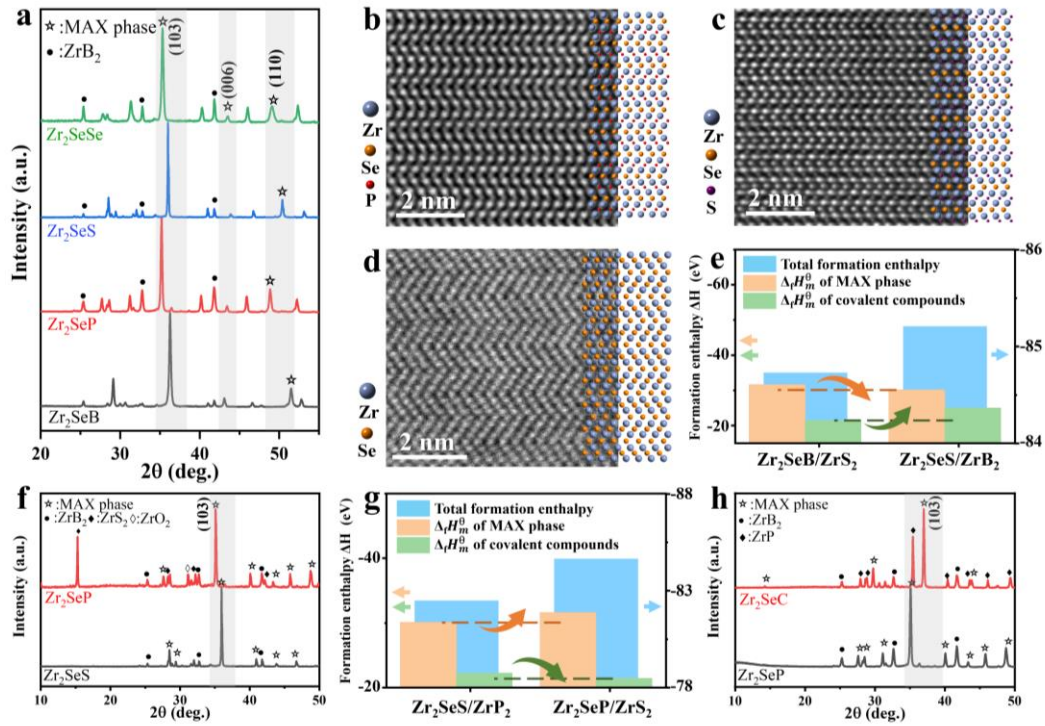


Fig. 2. Topochemical transformations among MAX phases utilizing covalent chemical scissors. (a) XRD patterns of Zr₂SeP, Zr₂SeS and Zr₂SeSe and their parent phase Zr₂SeB. (b-d) STEM images of Zr₂SeP, Zr₂SeS, and Zr₂SeSe along the [11 $\bar{2}$ 0] zone axis with their atomic structural models, respectively. (e) Formation enthalpy of reactants and products involved in the transformation of Zr₂SeB to Zr₂SeS. (f) XRD patterns of Zr₂SeP and its parent phase Zr₂SeS. (g) Formation enthalpy of reactants and products involved in the transformation of Zr₂SeS to Zr₂SeP. (h) XRD patterns of Zr₂SeC and its parent phase Zr₂SeP.

Substitution of Covalent [M-X] sublayers within MAX phases is mediated by covalent chemical scissors. The covalent chemical scissors, ZrP₂, inducing molten state (Table S5) at reaction temperature can promote the diffusion of activated ions through a solid-state matrix, as shown in Eqs. S1-S3 (Figs. 2a-b and S2). The ionized P²⁻ oxidizes the Zr atoms within Zr₂SeB (Figs. S2d, e and S3c). New Zr₂SeP MAX phase consequently forms and releases B²⁻. Then ultra-stable ZrB₂ rapidly nucleates as soon as B²⁻ diffuses out from the MAX phase matrix and interacts with surrounding Zr⁴⁺. This precipitation of ZrB₂ lowers the Gibbs free energy of the reaction system (Fig. 2e). Similarly, Se and S can selectively substitute B within Hf₂SB, Zr₂SeB, and Hf₂SeB using the corresponding chalcogenide chemical scissors, ZrSe₂, HfS₂, and

HfSe₂. A variety of MAX phases including Zr₂SeP, Hf₂SP, Hf₂SeP, Zr₂SeS, and Hf₂SeS have been successfully synthesized, as shown in Eqs. 1 and S4-S7 (Figs. S2, and S4-S7). The crystal structures of these newly formed MAX phases were thoroughly characterized using X-ray diffraction (XRD) aided with Rietveld refinement, scanning transmission electron microscopy (STEM), energy dispersive spectroscopy (EDS), and X-ray photoelectron spectroscopy (XPS). In the XRD pattern of Zr₂SeP, the (110) peak shifts to a lower Bragg angle as compared with Zr₂SeB precursor (Fig. 2a), indicating an expansion of the lattice parameter *a* from 3.561 Å to 3.735 Å. This anticipated increase is attributed to the enlargement of the [Zr-X] sublayers, where the smaller B (97 pm) is replaced by the larger P (109 pm). The distortion of the [Zr₆X] octahedron is reduced due to the smaller size difference (SD) between the stacked atoms (SD_{Zr-B}=61 pm, and SD_{Zr-P}=49 pm). Notably, the changes in the parameter *c* (0.5~0.8%) are significantly less pronounced than those observed for *a* (3~5%) when separately comparing Zr₂SeP, Hf₂SeP, and Hf₂SP to Zr₂SeB, Hf₂SeB, and Hf₂SB (Table S2). Consequently, the M-A bond length influenced by the expanded *a* and relatively invariable *c* elongates during the topochemical transformation, leading to a weakening of the M-A bond comprised of identical atoms (Fig. S1). Despite the increased formation enthalpy of the edited MAX phase, the stability of the metal boride and the resultant reduction in the total Gibbs free energy of the products facilitate the topochemical transformation (Fig. 2e). The typical mirrored zig-zag arrangements of the MAX phases were observed using the atom-resolved high-angle annular dark-field (HAADF) technique in STEM (Fig. 2b-c). EDS and XPS analyses further confirmed the incorporation of substituted non-metallic elements in the as-edited MAX phase (Figs. S2-S7).



MAX phases are usually considered as ternary compounds due to the constraints associated with the X-site constituents (usually C, N, B)²². While Se has been identified as a suitable X-site occupant in the $Zr_2Se(B_{1-x}Se_x)$, the thermodynamically stable binary compound Zr_2SeSe has not been successfully synthesized using the same powder metallurgical techniques applied to $Zr_2Se(B_{1-x}Se_x)$ ^{23,24}. In this study, we utilized covalent chemical scissors, specifically $ZrSe_2$, which shares the same anion as the A-site element in the Zr_2SeB precursor (Fig. S8). The inherent twinned $[Zr_6Se]$ triangular prism sublayers provide an architecture for the formation of Zr_2SeSe , thereby mitigating the need for excessive thermal energy during nucleation¹. Furthermore, competing phases such as Zr_2Se_3 and Zr_3Se_2 can be effectively eliminated through a straightforward topochemical transformation²³ (Eq. S8). Accordingly, other binary MAX phases, including Hf_2SS and Hf_2SeSe , were also achieved using HfS_2 and $HfSe_2$ as chemical scissors to tailor the Hf_2SB and Hf_2SeB precursors, respectively (Eqs. S9-S10) (Figs. S9-S10). In binary MAX phases, the $[M_6X]$ octahedron exhibits a more regular configuration, and the alleviation of octahedral distortion leads to reduced discrepancies in atomic arrangements and conduction behavior along the *a* and *c* axes (Fig. 2d)²³.

In addition to the $[M-X]$ sublayers derived from boride MAX phases, the new covalent $[M-X]$ sublayers can be further substituted through the application of covalent chemical scissors, following the sequence of Se, S, P, and C. For example, Zr_2SeC can be transformed from Zr_2SeB precursor by sequentially utilizing ZrS_2 , ZrP_2 and ZrC , as illustrated in Eqs. S4 and S11-S12 (Figs. 1b, 2f-h, and S11). In these reactions, the lower formation enthalpy ($Zr_2SeSe \approx Zr_2SeS > Zr_2SeP > Zr_2SeC$) determined by the stronger MX bonds within as-edited MAX phase plays a predominant role (Table S4). The resultant thermodynamically stable MAX phase,

following this editing process, is deemed suitable for high-temperature applications. However, the substitution process involving S and Se does not demonstrate a distinct substitution relationship. This is attributed to the comparable binding energies and valence states of these two elements when they occupy the X site in conjunction with the metal M. Instead, the decrease in free energy influenced by entropy changes, facilitates the mixing of S and Se at the X site, leading to the formation of $\text{Hf}_2\text{Se}(\text{S}_{0.5}\text{Se}_{0.5})$ (Fig. S12). Furthermore, a multi-principal MAX phase, $\text{Hf}_2\text{Se}(\text{S}_{0.25}\text{Se}_{0.25}\text{P}_{0.25}\text{B}_{0.25})$, has been successfully synthesized (Fig. S13). The grain size (~submicron) is quite small because of the refinement by the precipitation of HfB_2 which impedes the migration of grain boundaries within the MAX phase (Figs. S3a, d, g and S13b). Additionally, chalcogens exhibit a preferential occupancy at the A site when they coexist during the reaction. The anticipated Hf_2SSe could not be synthesized using HfSe_2 as chemical scissors to tailor the Hf_2SB precursor; instead, Hf_2SeS was successfully obtained, analogous to the products derived from the $\text{Hf}_2\text{SeB-HfS}_2$ reactants, as shown in Eqs. S13-S14 (Fig. S14). Lattice parameters calculated via first-principles methods indicate a significant distortion in the Hf_2SSe lattice as compared with Hf_2SeS . Consequently, Hf_2SSe spontaneously converts to Hf_2SeS due to the considerably lower in-plane energy of the latter under the similar total energy (Table S4). This observation suggests that the covalent chemical scissors can effectively customize not only the [M-X] sublayers but also the [M-A] sublayers within covalent MAX phases.

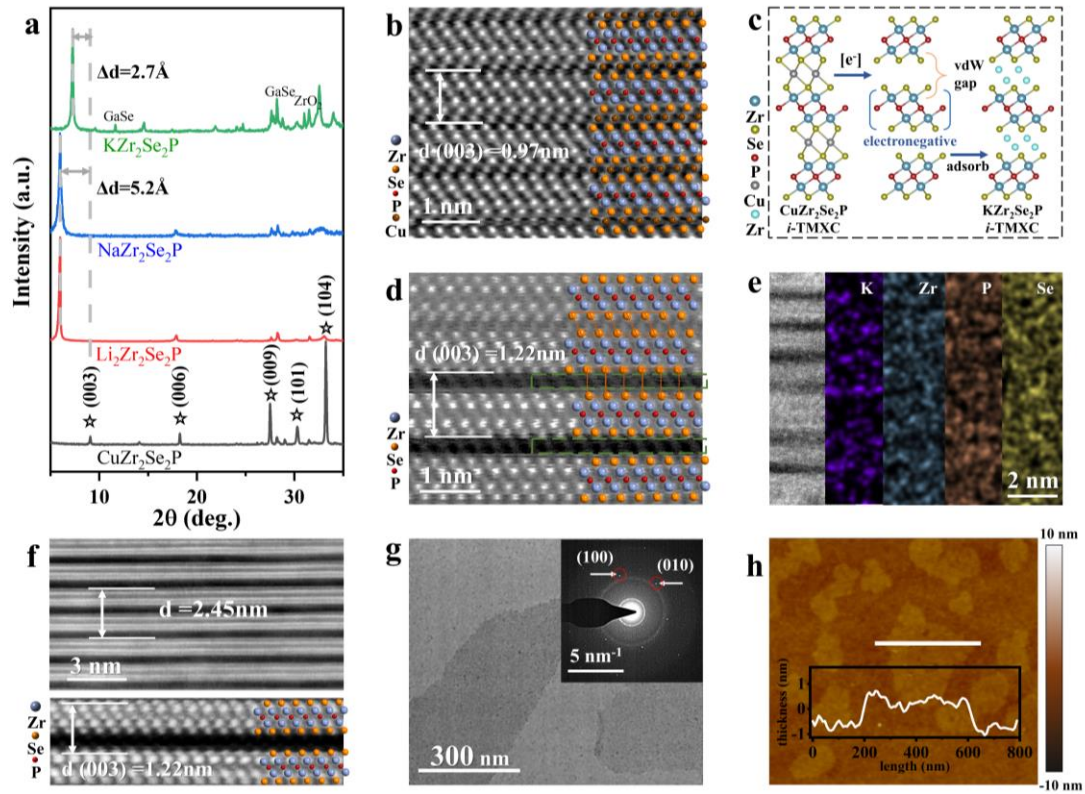
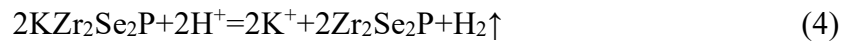


Fig. 3. The intercalation and deintercalation of Zr_2Se_2P . (a) XRD patterns of alkali metals intercalated Zr_2Se_2P and their parent phase $CuZr_2Se_2P$. (b) STEM image showing atomic arrangements of $CuZr_2Se_2P$ along $[110]$ direction, respectively. (c) Gap-opening mechanism of i -TMXC through Ga scissor. (d-e) STEM image along $[110]$ direction with EDS mapping of KZr_2Se_2P . (f) STEM image showing atomic arrangements of Zr_2Se_2P . (g) TEM images of Zr_2Se_2P single sheet. The inset shows the corresponding selected area electron diffraction pattern. (h) Atomic force microscope image of Zr_2Se_2P single sheet.

Topotactic structural transformation from MAX phase to TMXC is aided by intercalation and deintercalation. The covalent MAX phases, upon X-site modification, significantly influence the composition of $[M-X]$ sublayers²⁵. This alteration serves as a foundation for the synthesis of MXene-like materials, which exhibit distinctive properties linked to M-X orbital interactions. Unfortunately, the delamination of covalent MAX phases into 2D materials is infrequently achieved. The vdW multilayered transition metal carbo-chalcogenides (TMCC) can be obtained from carbide MAX phases through a sequential process involving S oxidation and Cu intercalation; their delamination is challenging due to limited interlamellar spacing²⁶.

Michael Naguib et al introduced an electrochemical lithiation technique to facilitate the swelling of multilayered Nb₂S₂C and Ta₂S₂C, enabling their delamination into individual sheets²⁷. In this work, LAMS is employed to intercalate foreign Cu and chalcogen into the covalent MAX phase precursors, resulting in formation of *i*-TMXC. The multilayered *i*-TMXC is subsequently produced through the reduction of metal scissors in alkali molten salt, which concurrently expands the interlamellar spacing of TMXC. The TMXC nanosheets (*d*-TMXC) are then exfoliated through progressive oxidation of protons and physical delamination. For example, the topochemical transformation from Zr₂SeP to 2D Zr₂Se₂P is shown in Eqs. 2-4:



The ionized Cu²⁺ derived from LAMS scissors CuCl₂ exhibits a significant electron affinity and oxidizes the Zr within Zr₂SeP (Eqs. S15-S16). The resultant positively charged Zr₂SeP⁺ engages in Coulombic interactions with the surrounding Se²⁻ anion, leading to the formation of Zr₂SeP⁻ (Eq. S17). The reduced Cu⁺ intercalated into the solid matrix is contributed to the electrical neutrality of CuZr₂Se₂P (Eq. S18). Valence state analyses of Zr and Cu in Zr₂SeP, CuZr₂Se₂P, and CuSe, conducted through XPS and XFAS, elucidate the electron transfer mechanisms involved (Figs. S4d and S15e-g). Given that Zr is coordinated to both Se and P in the original MAX phase, the intercalation sites for the foreign Cu and Se can be categorized into two configurations: [Zr₆Se] and [Zr₆P]. However, the lower valence state of Zr in the [Zr₆Se], coupled with the comparatively weaker bond strength of Zr-Se relative to Zr-P interactions in the [Zr₆P], suggests a preference for intercalation at the [Zr₆Se] and reconstruct covalent [Zr-P-Se] sublayers (Fig. S15g and Table S4).

This preference is experimentally validated by the observation of alternating stacked new [Se₆Cu] octahedral sublayers alongside the native [Zr₆P] octahedral sublayers in STEM (Fig. 3b). The molar ratios of Cu:Zr:Se:P and the microscopic layered morphology further substantiate the topochemical transformation from Zr₂SeP to CuZr₂Se₂P (Fig. S15a-b). In addition, Zr₂SeP undergoes decomposition into ZrP and ZrSe₂ through the direct oxidation of Se; conversely, Zr₂SeTeP can be synthesized via the oxidation of Zr₂SeP by Te without the necessity of Cu (Fig. S16). Cu acts as an electron donor, mitigating the excessive oxidation of Zr by Se, which is characterized by high electronegativity. This phenomenon parallels the transformation observed from Nb₂SC to Nb₂S₂C, where Nb₂SC decomposes into NbC and NbS₂ when S serves as the oxidant²⁶. Therefore, the selection of an appropriate oxidant with a weaker electron affinity than the A-site element is critical for the successful intercalation.

In order to exfoliate the TMXC nanosheets, the interlamellar spacing of CuZr₂Se₂P is opened through the reduction of Ga metal scissors in conjunction with the concurrent intercalation of K⁺ in the molten salt. This process is analogous to the use of metal scissors for the removal of terminations from MXenes and the intercalation of metals in transition metal dichalcogenides (TMDC)^{12, 27}. The electron donated from Ga reduces the Cu⁺ within CuZr₂Se₂P and Zr₂Se₂P⁻ consequently forms (Eqs. S19-S20). The surrounding K⁺ subsequently intercalates into the position previously occupied by Cu⁺ (Eqs. S21-S22) (Fig. 3c). Furthermore, the generation of low boiling-point GaCl₂ promotes the topochemical reaction and expands the interlamellar spacing (Eq. S23). The leftward shift of the (003) XRD peak indicates a successful topotactic structural transformation from CuZr₂Se₂P to KZr₂Se₂P (Fig. 3a). The SEM image of the fully etched CuZr₂Se₂P exhibits a characteristic accordion-like morphology, and EDS data confirms the complete removal of interlayer Cu and the

successful intercalation of K (Fig. S17a-b). The STEM image of K-intercalated Zr_2Se_2P demonstrates a significant increase in interlayer spacing, with the interplanar distance of (003) expanding from 0.97 nm to 1.22 nm. This observation aligns with the XRD results, and EDS mapping further corroborates the intercalation of K between the Zr_2Se_2P single layers (Fig. 3d, e). This methodology is broadly applicable for the intercalation of other alkali metals, such as Li and Na (Eqs. S24-S25). The resulting Li or Na intercalated TMXCs exhibit a greater swelling of (003) (5.2 Å) as compared with that of KZr_2Se_2P (2.7 Å) (Figs. 3a and S18). Notably, XFAS analysis indicates that the valence state of Zr in Li intercalated Zr_2Se_2P is equivalent to that in Zr_2Se_2P , but lower than in $CuZr_2Se_2P$, KZr_2Se_2P and $NaZr_2Se_2P$ (Fig. S18f). This suggests that a greater amount of Li^+ ions can be intercalated into the Zr_2Se_2P matrix as compared with the latter three. This finding implies that diverse intercalated TMXCs can be achieved through the mediation of molten salts with varying coordination environments of metallic cations^{28, 29}. The Zr_2Se_2P nanosheets were obtained from the oxidation of KZr_2Se_2P using protons and physical delamination. The reaction of H^+ with KZr_2Se_2P generates hydrogen gas (H_2), and facilitates the removal of alkali metal ions from the vdW gap of the Zr_2Se_2P layers (Fig. 3f). This interlayer hydrogen evolution induce further swelling of multilayered Zr_2Se_2P , ultimately leading to the delamination process into Zr_2Se_2P nanosheets (~monolayer) (Fig. 3g-h)³⁰. Unlike the typical MXenes derived from the exfoliation of metallic A-site elements within MAX phases, which are characterized by a single selenium termination³¹, 2D Zr_2Se_2P exhibits double selenium terminations on its surface, indicating a higher oxidation state of Zr. Consequently, these 2D TMXCs, which involve previous TMCC, can be classified as oxidized MXenes. This approach enables the creation of diverse 2D TMXCs with dual anions (XC). The modification

of orbital coupling within the [M-X] octahedral sublayers prompted by the terminations, is anticipated to yield intriguing properties in 2D materials. For example, the various interaction modes between alkali metals and Se regulated by [M-X] sublayers, suggesting that TMXC may be employed as a cathode material for alkali metal/Se batteries³². The band gap exceeding 1.5 eV found in the $\text{Li}_2\text{Zr}_2\text{Se}_2\text{P}$ indicates its application as optoelectronic devices (Fig. S19).

Conclusion: In summary, we have developed a methodology that employs chemical scissors to edit the covalent sublayers of nanolaminated early transition metal compounds, specifically MAX phases and *i*-TMXCs. The composition of the covalent [M-X] sublayers within MAX phases is precisely regulated through the covalent chemical scissors. Additionally, unconventional elements (such as Se, S, and P) are substituted into the X site of MAX phases via topochemical transformation, a process that is not feasible with traditional powder metallurgy techniques. The resulting 2D TMXCs, which incorporate two anions and are derived from the tailored covalent MAX phases successively using LAMS and metal scissors, exhibit unique structural characteristics akin to both MXenes and transition metal chalcogenides. This advancement significantly expands the family of 2D materials. Considering the diverse coordination environments present within TMXCs, further investigations may reveal intriguing physical properties, which could lead to progress in fields ranging from optoelectronics to energy storage.

References and Notes

1. Stein A, Keller SW, Mallouk TE. Turning down the heat: design and mechanism in solid-state synthesis. *Science* 1993, **259**(5101): 1558-1564.
2. Xu Y, Cao H, Xue Y, Li B, Cai W. Liquid-phase exfoliation of graphene: an overview on exfoliation media, techniques, and challenges. *Nanomaterials* 2018, **8**(11): 942.
3. Ricciardulli AG, Yang S, Smet JH, Saliba M. Emerging perovskite monolayers. *Nature Materials* 2021, **20**(10): 1325-1336.
4. Sahoo DP, Das KK, Mansingh S, Sultana S, Parida K. Recent progress in first

- row transition metal Layered double hydroxide (LDH) based electrocatalysts towards water splitting: A review with insights on synthesis. *Coordination Chemistry Reviews* 2022, **469**: 214666.
5. VahidMohammadi A, Rosen J, Gogotsi Y. The world of two-dimensional carbides and nitrides (MXenes). *Science* 2021, **372**(6547): eabf1581.
 6. Sokol M, Natu V, Kota S, Barsoum MW. On the chemical diversity of the MAX phases. *Trends in Chemistry* 2019, **1**(2): 210-223.
 7. Barsoum MW. The $M_{N+1}AX_N$ phases: A new class of solids: Thermodynamically stable nanolaminates. *Progress in solid state chemistry* 2000, **28**(1-4): 201-281.
 8. Naguib M, Kurtoglu M, Presser V, Lu J, Niu J, Heon M, *et al.* Two-dimensional nanocrystals: two-dimensional nanocrystals produced by exfoliation of Ti_3AlC_2 (Adv. Mater. 37/2011). *Advanced Materials* 2011, **23**(37): 4207-4207.
 9. Fashandi H, Dahlqvist M, Lu J, Palisaitis J, Simak SI, Abrikosov IA, *et al.* Synthesis of Ti_3AuC_2 , $Ti_3Au_2C_2$ and Ti_3IrC_2 by noble metal substitution reaction in Ti_3SiC_2 for high-temperature-stable Ohmic contacts to SiC. *Nature materials* 2017, **16**(8): 814-818.
 10. Li M, Lu J, Luo K, Li Y, Chang K, Chen K, *et al.* Element replacement approach by reaction with Lewis acidic molten salts to synthesize nanolaminated MAX phases and MXenes. *Journal of the American Chemical Society* 2019, **141**(11): 4730-4737.
 11. Li Y, Shao H, Lin Z, Lu J, Liu L, Duployer B, *et al.* A general Lewis acidic etching route for preparing MXenes with enhanced electrochemical performance in non-aqueous electrolyte. *Nature Materials* 2020, **19**(8): 894-899.
 12. Ding H, Li Y, Li M, Chen K, Liang K, Chen G, *et al.* Chemical scissor-mediated structural editing of layered transition metal carbides. *Science* 2023, **379**(6637): 1130-1135.
 13. Wang Y, Li L, Shen M, Tang R, Zhou J, Han L, *et al.* Simple One-Step Molten Salt Method for Synthesizing Highly Efficient MXene-Supported Pt Nanoalloy Electrocatalysts. *Advanced Science* 2023, **10**(33): 2303693.
 14. Li D, Zheng W, Gali SM, Sobczak K, Horák M, Polčák J, *et al.* MXenes with ordered triatomic-layer borate polyanion terminations. *Nature Materials* 2024: 1-8.
 15. An Y, Tian Y, Shen H, Man Q, Xiong S, Feng J. Two-dimensional MXenes for flexible energy storage devices. *Energy & Environmental Science* 2023, **16**(10): 4191-4250.
 16. Jiang M, Wang D, Kim YH, Duan C, Talapin DV, Zhou C. Evolution of Surface Chemistry in Two-Dimensional MXenes: From Mixed to Tunable Uniform Terminations. *Angewandte Chemie* 2024: e202409480.
 17. White KE, Chu YZ, Gani G, Ippolito S, Barr KK, Thomas JC, *et al.* Atomic-scale investigations of Ti_3C_2Tx MXene surfaces. *Matter* 2024, **7**(7): 2609-2618.
 18. Ali M, Hossain M, Uddin M, Hossain M, Islam A, Naqib S. Physical properties of new MAX phase borides M_2SB (M= Zr, Hf and Nb) in comparison with conventional MAX phase carbides M_2SC (M= Zr, Hf and Nb): Comprehensive insights. *Journal of Materials Research and Technology* 2021, **11**: 1000-1018.

19. Rackl T, Eisenburger L, Niklaus R, Johrendt D. Syntheses and physical properties of the MAX phase boride Nb₂SB and the solid solutions Nb₂SB_xC_{1-x} (x=0–1). *Physical Review Materials* 2019, **3**(5): 054001.
20. Chen K, Bai X, Mu X, Yan P, Qiu N, Li Y, *et al.* MAX phase Zr₂SeC and its thermal conduction behavior. *Journal of the European Ceramic Society* 2021, **41**(8): 4447-4451.
21. Zhang Q, Zhou Y, San X, Wan D, Bao Y, Feng Q, *et al.* Thermal explosion synthesis of first Te-containing layered ternary Hf₂TeB MAX phase. *Journal of the European Ceramic Society* 2023, **43**(1): 173-176.
22. Dahlqvist M, Barsoum MW, Rosen J. MAX phases—Past, present, and future. *Materials Today* 2024, **72**: 1-24.
23. Li Z, Wu E, Chen K, Wang X, Chen G, Miao L, *et al.* Chalcogenide MAX phases Zr₂Se(B_{1-x}Se_x)(x= 0–0.97) and their conduction behaviors. *Acta Materialia* 2022, **237**: 118183.
24. Hadi MA, Akhter M, Ahasan MS, Ahmed I, Kashem MA. Realization of diversity in physical properties of Zr₂Se(B_{1-x}Se_x) MAX phases through DFT approach. *Journal of the American Ceramic Society* 2023, **106**(10): 6177-6193.
25. Zhou J, Palisaitis J, Halim J, Dahlqvist M, Tao Q, Persson I, *et al.* Boridene: Two-dimensional Mo_{4/3}B_{2-x} with ordered metal vacancies obtained by chemical exfoliation. *Science* 2021, **373**(6556): 801-805.
26. Sakamaki K, Wada H, Nozaki H, Ōnuki Y, Kawai M. Topochemical formation of van der Waals type niobium carbosulfide 1T-Nb₂S₂C. *Journal of alloys and compounds* 2002, **339**(1-2): 283-292.
27. Majed A, Kothakonda M, Wang F, Tseng EN, Prenger K, Zhang X, *et al.* Transition Metal Carbo-Chalcogenide “TMCC:” A New Family of 2D Materials. *Advanced Materials* 2022, **34**(26): 2200574.
28. Chen B, Chao D, Liu E, Jaroniec M, Zhao N, Qiao S-Z. Transition metal dichalcogenides for alkali metal ion batteries: engineering strategies at the atomic level. *Energy & Environmental Science* 2020, **13**(4): 1096-1131.
29. Wang Z, Selbach SM, Grande T. Van der Waals density functional study of the energetics of alkali metal intercalation in graphite. *Rsc Advances* 2014, **4**(8): 4069-4079.
30. Viculis LM, Mack JJ, Mayer OM, Hahn HT, Kaner RB. Intercalation and exfoliation routes to graphite nanoplatelets. *Journal of Materials Chemistry* 2005, **15**(9): 974-978.
31. Kamysbayev V, Filatov AS, Hu H, Rui X, Lagunas F, Wang D, *et al.* Covalent surface modifications and superconductivity of two-dimensional metal carbide MXenes. *Science* 2020, **369**(6506): 979-983.
32. Eftekhari A. The rise of lithium–selenium batteries. *Sustainable energy & fuels* 2017, **1**(1): 14-29.